Meccanica (2019) 54:1083–1102
https://doi.org/10.1007/s11012-019-01013-3

Magnetically driven foldable shell type swimmers at Stokes flow

İzzet Özdemir

Received: 6 December 2018 / Accepted: 28 June 2019 / Published online: 10 July 2019

Abstract This paper focuses on the interaction of low Reynolds number (Re) flows and thin shell type deformable structures in the context of flexible body locomotion and addresses the coupled field problem through a numerical solution framework. The thin structure is discretized by enhanced three-node finite elements and coupled with boundary element based treatment of Stokes flow in a monolithic manner. The locomotion is triggered and driven by an external magnetic field that generates displacement dependent body couples over the magnetically sensitive parts of the flexible structure. A particular novelty of the paper is the use of internal hinges through which very large rotations and structural deformations can be combined in an efficient way. Using this concept; new, on the fly locomotion direction reversal mechanisms can be generated as demonstrated by the foldable bi-directional swimmer.

Keywords Fluid–structure interaction · Low Reynolds number flows · Finite element method · Boundary element method

İ. Özdemir (✉)
Department of Civil Engineering, İzmir Institute of Technology, Gülbahçe Kampüsü, Urla, İzmir, Turkey
e-mail: izzetozdemir@iyte.edu.tr

1 Introduction

The physics of swimming at very small length scales is an active field of research due to its impact on biomedical and microfluidics applications, see e.g. [1]. Since inertia forces are negligible at such small scales, the flow is essentially governed by the viscous forces and the resulting flow is classified as low Reynolds number (Re) flow. In the limit of zero Re, the flow is called as Stokes flow and governed by a pair of linear partial differential equations. Unraveling the hydrodynamics of sperm and many other micro-organisms [2], development of artificial micro-swimmers necessitate a proper understanding of fluid–structure interaction at low Re flows.

Fluid–structure interaction (FSI) at low Re flows have distinct characteristics and in fact they are stemming from the linearity and reversibility of the flow, see e.g. [2]. Probably the most striking example reflecting the peculiar nature of FSI at low Re flows is the fact that conducting a set of time symmetric movements (reciprocal motion) does not result in any net translation of the body, see [3]. In order to break time symmetry, a typical strategy is to adopt chiral shapes such as helical geometries. Imposing time irreversible undulating body profiles is another way of achieving translation in a specific direction. For certain strategies, to achieve net translation within the surrounding viscous fluid, a vital component is the flexibility of the body and the intimate interplay developing between elastic and viscous forces.

Therefore, when the deformable body is partially controlled or has some passive elastic components, deformations have to be taken into account in a rigorous way.

The simplest analysis framework for fluid-deformable slender body interaction in Stokes flow was proposed by Gray and Hancock which is known as the Resistive Force Theory (RFT), see [4]. In this theory, the fluid resistance is accounted for in the form of velocity proportional local drag forces exerted on the slender body. The hydrodynamic interaction between different parts of the body is ignored. In many cases, RFT yields satisfactory results provided that the resistance coefficients are calibrated properly. However, as reported by Rodenborn et al. [5], for 3D helical swimmers with certain geometries (e.g. relatively small pitches), the predictions of RFT are unsatisfactory.

In order to capture the hydrodynamic interactions, so called slender body theories were proposed where the flow induced by the motion of a slender body is represented by distributed point forces and source dipoles along the center line of the rod like bodies, see [6, 7]. These theories can be put into a non-singular integral form with a proper choice of dipole density and they naturally capture the hydrodynamic interactions between different parts. Their predictive capacities are better than RFT as documented in [5].

As presented briefly in Sect. 2, Stokes flow is governed by a pair of linear differential equations for which the free space fundamental solution is available, see [8]. Utilizing this solution in combination with superposition principle and interface conditions (e.g. no slip between the fluid (flow) and the structure), arbitrary fluid tractions are injected into the variational form of the linear momentum balance for the slender body. To address the integration of singular kernels, Cortez introduced the method of regularized Stokeslet in which a non-singular kernel is obtained by replacing the point load with a smooth function that has a narrow support controlled by a regularization parameter, see [9, 10]. The method is closely related to the boundary element method and proper selection of the regularization parameter is very critical to obtain sufficiently accurate predictions. In fact, a truly BEM type treatment of the Stokes flow is combined with both 2D and 3D finite element based structural models and solved implicitly in a monolithic manner as presented in [11–13]. These models were very instrumental to investigate the mechanics of swimming and mixing at small scales including the magnetically actuated artificial cilia and swimming direction reversal strategies.

Apart from hydrodynamics of slender bodies, an efficient power supply and control concept seems to be an important unsolved issue as far as man-made micro-swimmers are concerned, see [14, 15]. On-board power supplies are not very desirable due to limitations on their miniaturization. One of the potential remedies investigated by different groups is the use of magnetic actuation through external magnets to remotely actuate micro-swimmers. This solution is also an attractive option in biomedical applications, since the required magnetic field intensities are relatively low and harmless to cells and tissues, see e.g. [16]. It is also reported that magnetic actuation is much more controllable as compared to other mechanisms, see [17].

Therefore reliable predictive tools for magnetically driven flexible micro-swimmers would be valuable additions to the set of tools to analyze different geometric lay-outs and motion control scenarios. In fact, inducing and reversing a helix like chiral shape on a flat thin strip by means of an external magnetic field has been successfully used to control the swimming direction (in the sense of forward or backward) on the fly. In addition to symmetry breaking chiral geometries, swimming direction can also be controlled by ‘folding’ the structure in an efficient way, for instance by means of internal hinges as shown in Sect. 3. Furthermore, such hinge mechanisms would be very instrumental in combining active and passive elastic components within the same structure which in turn would enrich the design space of artificial micro-swimmers.

Motivated by these ideas, in this paper a coupled finite element–boundary element monolithic solution framework is implemented to address the mechanics of the locomotion of thin shell type structures in Stokes flow. In the next section, problem formulation is given with concise treatment of structural and flow models including interface conditions, injection of internal hinges and magnetically induced body couples. Section 3 focuses on a new type of ‘foldable’ swimmer with swimming direction reversal capability. Using the implemented framework, swimming direction reversibility is demonstrated and the influence of different parameters on swimming

performance is presented with a non-dimensional perspective. The paper is closed by conclusion and outlook section followed by an "Appendix" reserved for certain details of the numerical implementation, validation of individual field solvers and dimensional analysis.

2 Problem formulation

Thin and slender deformable swimmer is composed of two flat thin strips connected by a relatively short middle piece through internal hinges. Grey regions are the magnetically sensitive parts of the structure and the arrows indicate the initial remnant magnetization direction. The boundaries of the surrounding fluid domain are located sufficiently far away as compared to the length of the body so that the fluid domain is assumed to be infinitely large in all directions.

The body is going to be propelled by magnetically induced body couples (acting over sensitive sub-parts) created by an externally applied (varying) magnetic field. When the body is perturbed by means of these distributed couples, the surrounding fluid is going to exert drag forces on the swimmer. An equal and opposite force is going to disturb the surrounding fluid domain initializing and fostering a flow field. As discussed in Sect. 3, by splitting the external magnetic loading protocol into phases, the 'arms' of the swimmer can be aligned with a specific direction (e.g. + z or − z direction, see the right hand-side of Fig. 1) and afterwards undulating deformation profiles can be induced by oscillating the external magnetic field. Obviously the resulting motion of the slender body involves large displacements and rotations. Therefore, geometrically nonlinear continuum mechanics framework is adopted and Newton–Raphson based incremental-iterative solution procedure is used to solve the resulting coupled problem.

In the following subsections, the structural model, the flow model, the treatment of the magnetically induced body couples and coupling of structural and flow fields in a monolithic framework are going to be presented separately.

2.1 Structural model

Shear deformable, mid-surface based shell model is used to describe the structural response. Shear deformable theory (Reissner–Mindlin kinematics) is preferred primarily due to lower continuity requirements. Since arbitrarily large displacements and rotations can be conveniently addressed by the finite element (FE) method, the rest of this section focuses on the shell element formulation including the treatment of kinematical constraints induced by an internal hinge. The element used in this work is the enhanced triangular element (triangular MITC3+ element, presented in [18, 19]) which belongs to the family of MITC shell elements.

Before embarking on the variational basis of the problem, basic kinematical features of the element are briefly presented. A more detailed treatment is available in [18, 19]. As shown in Fig. 2, the element has three corner nodes and an interior node. In order to describe the rotation field, at each node a director vector and two additional vectors $\mathbf{V}_1^i$ and $\mathbf{V}_2^i$ (orthogonal to the director) are introduced. Corner nodes have three translational degrees of freedom and two rotational ones whereas the interior node is equipped with only two rotational degrees of freedom. At node i, the incremental rotation around $\mathbf{V}_1^i$ and $\mathbf{V}_2^i$ vectors are

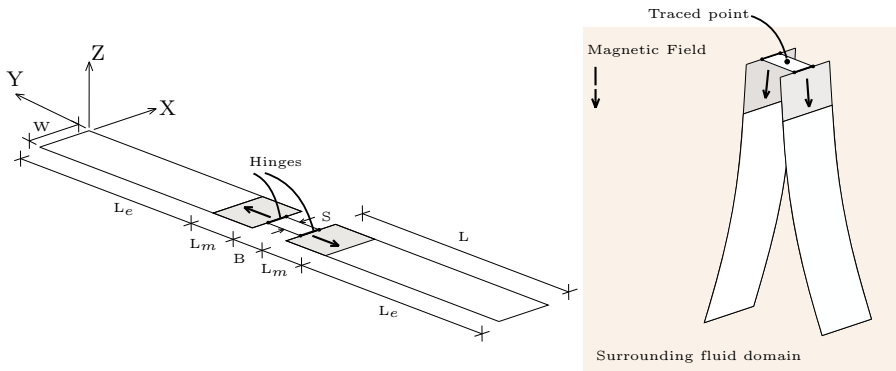

Fig. 1 Geometry of the foldable swimmer (left) and large rotations of the arms under an external magnetic field (right). The magnetic parts tend to align with the external magnetic field. Position history of the traced point is used to calculate the average velocity of the swimmer in Sect. 3

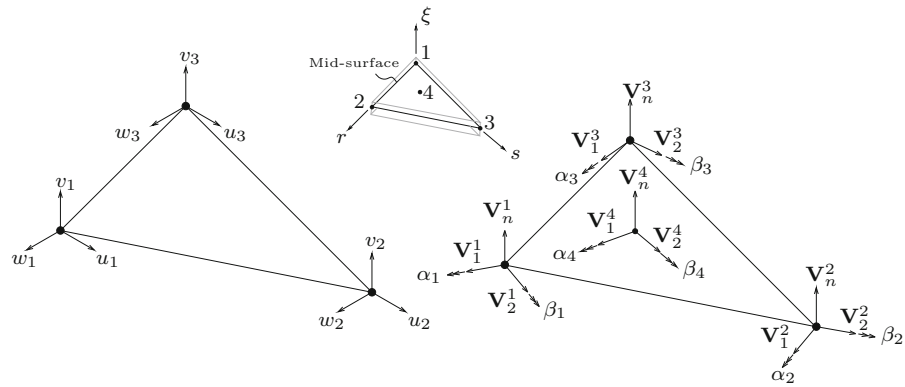

Fig. 2 Triangular mid-surface based shell element, left: displacement degrees of freedom defined at the corner nodes, right: vector triads defined at each node and the associated rotational degrees of freedom

expressed by nodal degrees of freedom α^i and β^i, respectively.

In a geometrically nonlinear setting, the position vector $\mathbf{x}$ of any material point within the element at time t and the incremental displacement vector $\mathbf{u}$ (from t to t + Δt) are expressed as,

$$\mathbf{x} = \sum_{i=1}^{3} h_i(r,s)\mathbf{x}_i + \frac{\xi}{2}\sum_{i=1}^{4} a_i f_i(r,s)\mathbf{V}_n^i \tag{1}$$

$$\mathbf{u} = \sum_{i=1}^{3} h_i(r,s)\mathbf{u}_i + \frac{\xi}{2}\sum_{i=1}^{4} a_i f_i(r,s)\left(\mathbf{V}_n^{i,t+\Delta t} - \mathbf{V}_n^{i,t}\right) \tag{2}$$

$$\text{with } a_4\mathbf{V}_n^4 = \frac{1}{3}\left(a_1\mathbf{V}_n^1 + a_2\mathbf{V}_n^2 + a_3\mathbf{V}_n^3\right) \tag{3}$$

$$\text{and } h_1 = 1.0 - r - s; h_2 = r; h_3 = s \tag{4}$$

in which shell thickness and the director vector at each node are represented by a_i and $\mathbf{V}_n^i$, respectively. ξ is the (curvilinear) coordinate in the thickness direction and $f_i(r,s)$ are the interpolation functions for the rotation field. The particular form of f_4 resembles the bubble function and these functions read as,

$$\begin{aligned} &f_1 = h_1 - 1/3 f_4; f_2 = h_2 - 1/3 f_4; \\ &f_3 = h_3 - 1/3 f_4; f_4 = 27\, r\, s\, (1 - r - s) \end{aligned} \tag{5}$$

It is important to note that the geometry of the element remains planar and the rotational degrees of freedom associated with the internal node do not influence the stretching and in-plane shear strains.

The update of the director vector from configuration t to $t + \Delta t$ is done by means of the rotation tensor $\mathbf{Q}$ through,

$$\mathbf{V}_n^{i,t+\Delta t} = \mathbf{Q}\mathbf{V}_n^{i,t} \tag{6}$$

Vector like parametrization of $\mathbf{Q}$ in terms of incremental rotations around $\mathbf{V}_1^{i,t}$ and $\mathbf{V}_2^{i,t}$ and its quadratic approximation through Taylor's series expansion leads to the following form for the incremental displacements,

$$\begin{aligned} \mathbf{u} = &\sum_{i=1}^{3} h_i(r,s)\mathbf{u}_i + \frac{\xi}{2}\sum_{i=1}^{4} a_i f_i(r,s) \\ &\times \left(-\alpha_i\mathbf{V}_2^{i,t} + \beta_i\mathbf{V}_1^{i,t} - \frac{1}{2}(\alpha_i^2 + \beta_i^2)\mathbf{V}_n^{i,t}\right) \end{aligned} \tag{7}$$

including the second order rotation effects. Update of the director vector at each node is done at the end of the increment upon satisfaction of the equilibrium equations. Once the director vector is updated through Eq. (6), $\mathbf{V}_1^{i,t+\Delta t}$ and $\mathbf{V}_2^{i,t+\Delta t}$ are updated using the orthogonality condition given as,

$$\mathbf{V}_1^{i,t+\Delta t} = \frac{\mathbf{e}_2 \times \mathbf{V}_n^{i,t+\Delta t}}{||\mathbf{e}_2 \times \mathbf{V}_n^{i,t+\Delta t}||} \tag{8}$$

$$\mathbf{V}_2^{i,t+\Delta t} = \mathbf{V}_n^{i,t+\Delta t} \times \mathbf{V}_1^{i,t+\Delta t} \tag{9}$$

In case $\mathbf{e}_2$ and $\mathbf{V}_n^{i,t+\Delta t}$ are collinear, $\mathbf{V}_1^{i,t+\Delta t}$ is set equal to $\mathbf{e}_3$.

Introducing the basis vectors $\mathbf{G}_i = \frac{\partial \mathbf{X}}{\partial r_i}$ and $\mathbf{g}_i = \frac{\partial \mathbf{x}}{\partial r_i}$ with $r_1 = r, r_2 = s, r_3 = \xi$; the covariant components of the Green–Lagrange strain tensor $\mathbf{E}$ are written as,

$$E_{ij} = \frac{1}{2}\left(\mathbf{g}_i \cdot \mathbf{g}_j - \mathbf{G}_i \cdot \mathbf{G}_j\right) \tag{10}$$

where $\mathbf{X}$ and $\mathbf{x}$ are the position vector at reference and current configurations, respectively. Although the displacements and rotations are large, the resulting

strains are supposed to be within the elastic range so that there is no permanent deformation upon hydrodynamic loading and load reversals. Therefore, it is assumed that the strains are sufficiently small such that a linear relation between $\mathbf{E}$ and 2nd Piola–Kirchhoff stress tensor $\mathbf{S}$ holds (St. Venant's Kirchhoff material); and the mechanical response is isotropic. Therefore contravariant stress components are obtained through,

$$\mathbf{S} = \mathbb{C} : \mathbf{E} \tag{11}$$

in which $\mathbb{C}$ is the fourth order elasticity tensor with contravariant components. Since elasticity tensor is typically defined with respect to a local basis defined at material point level ($\mathbb{C}_{local}$), it has to be properly transformed at each integration point. In fact, $\mathbb{C}_{local}$ is obtained from the full elasticity tensor by imposing the plane stress assumption along the thickness direction, i.e. zero normal stresses in thickness direction under arbitrary strain states, see [20].

The family of MITC elements uses the Mixed Interpolated Tensorial Components (MITC) scheme to circumvent shear locking as exemplified in [19]. Displacement based transverse shear strains are replaced by the following assumed strain (AS) interpolations,

$$E^{AS}_{r\xi} = \frac{2}{3}\left(E^{(B)}_{r\xi} - \frac{1}{2}E_{s\xi^{(B)}}\right) + \frac{1}{3}\left(E^{(C)}_{r\xi} + E^{(C)}_{s\xi}\right) + \frac{1}{3}\hat{c}(3\,s - 1) \tag{12}$$

$$E^{AS}_{r\xi} = \frac{2}{3}\left(E^{(A)}_{s\xi} - \frac{1}{2}E_{r\xi^{(A)}}\right) + \frac{1}{3}\left(E^{(C)}_{r\xi} + E^{(C)}_{s\xi}\right) + \frac{1}{3}\hat{c}(1 - 3\,r) \tag{13}$$

in which $\hat{c} = E^{(F)}_{r\xi} - E^{(D)}_{r\xi} - E^{(F)}_{s\xi} + E^{(E)}_{s\xi}$ and A, B, C, D, E, F are the tying positions and their coordinates are given in [18].

At this stage, it is appropriate to introduce the variational form of the problem which reads as,

$$\delta W_{int} = \delta W_{ext} \tag{14}$$

$$\text{with } \delta W_{int} = \int_{V_0} \mathbf{S} : \delta\mathbf{E}\, dV = \int_{V_0} S^{ij}\delta E_{ij}\, dV_0 \tag{15}$$

$$\text{and } \delta W_{ext} = \underbrace{\int_A \mathbf{t}^f \cdot \delta\mathbf{u}\, dA}_{\delta W_f} + \underbrace{\int_{V_m} \mathbf{q} \cdot \delta\boldsymbol{\phi}\, dV}_{\delta W_m} \tag{16}$$

where $\mathbf{t}^f$ and $\mathbf{q}$ are the fluid traction and magnetically induced body couples, respectively. A is the current mid-surface area and V_m is the current volume of the magnetically sensitive part of the structure. In accordance with the shell element formulation, it is assumed that the fluid traction is acting on the mid-surface. Virtual displacements are designated by $\delta\mathbf{u}$ and $\delta\boldsymbol{\phi}$ represents the virtual rotations with a vector like notation. Internal virtual work δW_{int} has to be evaluated over the undeformed volume of the shell V_0 and written in terms of 2nd Piola–Kirchhoff stress tensor $\mathbf{S}$ and Green–Lagrange strain tensor $\mathbf{E}$ in contravariant and covariant components, respectively. Variationally the problem is of mixed type due to assumed out of plane shear strains.

Having defined basic kinematics in a discrete setting, $\mathbf{E}$ and $\mathbf{S}$, the internal virtual work δW_{int} can be written as a summation of sub-integrals over elemental volumes as,

$$\delta W_{int} = \sum_{e=1}^{n_e} \delta\underline{u}_e^T \int_{-1}^{1}\int_{A_\triangle} (\underline{B}_L + \underline{B}_{NL})\,\underline{S}\,J_0\,J_\xi\, dA_\triangle\, d\xi \times = \sum_{e=1}^{n_e} \delta\underline{u}_e^T \underline{f}_{int} \tag{17}$$

where $\underline{B}_L$ and $\underline{B}_{NL}$ are the linear and non-linear parts of the strain-displacement matrices. For a detailed treatment, the reader can consult to [20, 21].

As presented in Sect. 3, a convenient way of imposing large rotations is to introduce an internal hinge along an arbitrary line within the structure. The hinge along an arbitrary line is described by an axis as shown in Fig. 3.

Such a hinge facilitates different rotations of the two sides of the structure and require a number of algorithmic modifications. Referring to Fig. 3, for the nodes located on the hinge axis, $\mathbf{V}_2$ is forced to be co-linear with the hinge axis throughout the motion. Furthermore, director vector $\mathbf{V}_n$, $\mathbf{V}_1$ vector and rotational degree of freedom associated with $\mathbf{V}_2$ of the nodes located on the hinge axis are duplicated such that each rotational dof, $\mathbf{V}_n$ and $\mathbf{V}_1$ are associated with one of the neighboring elements. Therefore neighbouring elements have distinct $\mathbf{V}_1$, $\mathbf{V}_n$ and rotational dof associated with $\mathbf{V}_2$ whereas the translational dofs and rotational dof associated with $\mathbf{V}_1$ are identical for the nodes located on the hinge axis. At the end of each

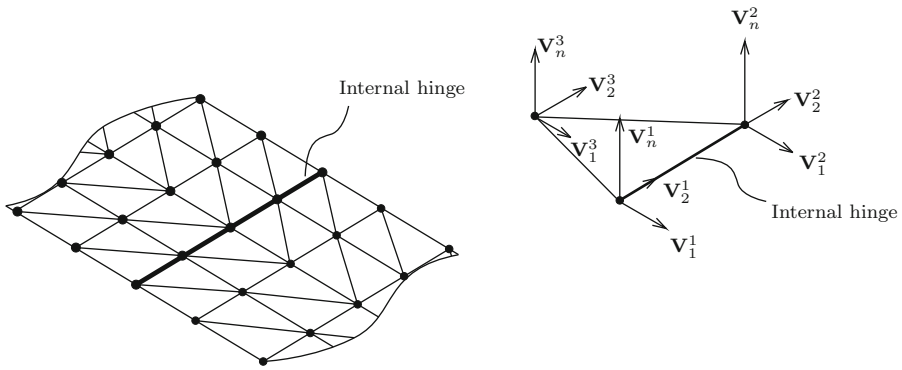

Fig. 3 Geometric layout of an internal hinge. Algorithmic updates of the triads of the nodes lying on the hinge are done in a different way

increment, the updated positions of the nodes located on the hinge axis are used to define $\mathbf{V}_2^{i,t+\Delta t}$ and by using the updated director vector $\mathbf{V}_n^{i,t+\Delta t}$, $\mathbf{V}_1^{i,t+\Delta t}$ is obtained through the orthogonality relation,

$$\mathbf{V}_1^{i,t+\Delta t} = \mathbf{V}_2^{i,t+\Delta t} \times \mathbf{V}_\mathbf{n}^{\mathbf{i},\mathbf{t}+\Delta\mathbf{t}} \tag{18}$$

The treatment of δW_{ext} is going to be presented in the following sub-sections.

2.2 Flow model and interface conditions

Incompressible Stokes flow is governed by the following equations,

$$\mu \nabla^2 \dot{\mathbf{u}}^f - \nabla p = 0 \tag{19}$$

$$\nabla \cdot \dot{\mathbf{u}}^f = 0 \tag{20}$$

where μ is the viscosity, $\dot{\mathbf{u}}^f$ and p are the velocity and pressure fields within the fluid domain, respectively. Physically the first equation reflects the balance of pressure gradient and viscous forces induced upon fluid motion and the second equation is the incompressibility constraint. The symbols ∇, $\nabla\cdot$ and ∇^2 represent the gradient, divergence and Laplace operators, respectively. As mentioned before, the fluid domain is extending to very large distances in all directions as compared to the structural dimensions and the structure acts as an internal boundary on which no-slip interface conditions,

$$\dot{\mathbf{u}}^f = \dot{\mathbf{u}}^s \text{ on } A \tag{21}$$

are imposed with $\dot{\mathbf{u}}^s$ representing the structural velocity field. Referring back to Stokes equations (equations 19), velocity field induced by a concentrated force $\mathbf{f}$ at position $\mathbf{x}^*$ in an infinite fluid medium (free space fundamental solution) is given by Pozrikidis [22] as,

$$\dot{\mathbf{u}}^f = \mathbf{G}\,\mathbf{f} \text{ with } G_{ij} = \frac{1}{8\pi\mu}\left(\frac{\delta_{ij}}{R} + \frac{R_i R_j}{R^3}\right) \tag{22}$$

where $\mathbf{R} = \mathbf{x} - \mathbf{x}^*$, $R = ||\mathbf{R}||$.

Replacing the concentrated force $\mathbf{f}$ with tractions $\mathbf{t}^s$ exerted by the structure over an infinitesimal area located on the interface (the mid-surface of the shell) and acting on the fluid domain, the fluid velocity field can be written as,

$$\dot{\mathbf{u}}^f = \int_A \mathbf{G}\,\mathbf{t}^s dA \tag{23}$$

Using the equilibrium condition,

$$\mathbf{t}^f = -\mathbf{t}^s \text{ on } A \tag{24}$$

where $\mathbf{t}^f$ is the traction exerted by the fluid on the structure, the following equation emerges,

$$\dot{\mathbf{u}}^f = -\int_A \mathbf{G}\,\mathbf{t}^f dA \tag{25}$$

Following [12], a linear interpolation for $\mathbf{t}^f$ in terms of nodal traction variables (over each element) is adopted and expressed as,

$$\underline{t}_e^f = \underline{N}\,\hat{\underline{t}}_e^f \tag{26}$$

$$\text{with } \left(\underline{\hat{t}}_e^f\right)^T = \begin{bmatrix} t_x^1 & t_y^1 & t_z^1 & t_x^2 & t_y^2 & t_z^2 & t_x^3 & t_y^3 & t_z^3 \end{bmatrix} \tag{27}$$

$$\text{and } \underline{N} = \begin{bmatrix} h_1 & 0 & 0 & h_2 & 0 & 0 & h_3 & 0 & 0 \\ 0 & h_1 & 0 & 0 & h_2 & 0 & 0 & h_3 & 0 \\ 0 & 0 & h_1 & 0 & 0 & h_2 & 0 & 0 & h_3 \end{bmatrix} \tag{28}$$

Inserting Eq. (26) into Eq. (25) and switching to a matrix-column notation, flow velocity field can be written as,

$$\underline{\dot{u}}^f = \sum_{e=1}^{n_e} - \int_{A_e} \underline{G}\,\underline{N}\,\underline{\hat{t}}_e^f \, dA_e \longrightarrow \underline{\dot{U}}^f = \underline{H}\,\underline{\hat{t}}^f \tag{29}$$

where an assembly operation in the usual finite element sense is implied by the summation sign resulting in system level matrices $\underline{H}$ and $\underline{\hat{t}}^f$. In a discrete setting no-slip interface condition can be expressed as,

$$\underline{\dot{U}}^f = \underline{A}\,\underline{\dot{U}}^s \tag{30}$$

where $\underline{A}$ is the constant matrix eliminating the rotational degrees of freedom of the structure. Therefore, the following equality holds,

$$\underline{A}\,\underline{\dot{U}}^s = \underline{H}\,\underline{\hat{t}}^f \tag{31}$$

and through an inversion operation, $\underline{\hat{t}}^f$ can be expressed solely in terms of $\underline{\dot{U}}^s$ as,

$$\underline{\hat{t}}^f = \underline{H}^{-1}\underline{A}\,\underline{\dot{U}}^s \tag{32}$$

Referring back to δW_{ext}, the first term can then be written as,

$$\begin{aligned} \int_A \delta\mathbf{u}\cdot\mathbf{t}^f \, dA = \sum_{e=1}^{n_e} \int_{A_e} \delta\underline{u}_e^T \underline{N}^T \underline{N}\,\underline{t}_e^f \, dA_e \\ \times = \delta\underline{\hat{u}}^T \underline{M}\,\underline{H}^{-1}\underline{A}\,\underline{\dot{U}}^s = \delta\underline{\hat{u}}^T \underline{f}_d \end{aligned} \tag{33}$$

in which $\underline{M}$ is the system level matrix resulting from element level contributions $\int_{A_e} \underline{N}^T\underline{N}\, dA_e$.

2.3 Magnetically induced body couples

The magnetic parts of the structure have certain remnant magnetization directions designated by $\mathbf{m}$. Imposition of external magnetic field $\mathbf{b}$ results in body couples given by $\mathbf{q} = m_r\,\mathbf{m}\times\mathbf{b}$ where m_r is the remnant magnetization of the sensitive parts. Under the action of these body couples, the magnetic parts tend to get aligned with the external magnetic field. In case of multiple magnetic parts on the same body, magnetic interactions between different parts are small for thin walled structures and can be discarded as demonstrated in [23]. Therefore, it is plausible to assume that the external magnetic field is uniform within the domain of interest (within both the fluid and structural domain) and prescribed externally. Magnetic parts are typically a small fraction of the total length. In fact, the propulsion results from an interplay between viscous, elastic and magnetic forces and increasing the length of magnetic parts beyond a limit would decrease the flexibility of the structure and some symmetry breaking, efficient body profiles can not be realized.

The remnant magnetization direction follows the deformation of the body and is essentially the material unit vector obtained through,

$$\mathbf{m} = \frac{\mathbf{F}_M\,\mathbf{m}_0}{||\mathbf{F}_M\,\mathbf{m}_0||} \tag{34}$$

where $\mathbf{m}_0$ is the initial magnetization direction. In fact uniformly distributed body couples result in a rigid body rotation type motion for the magnetically sensitive parts and therefore the influence of transverse shear deformations are negligibly small. Motivated by this observation, deformation gradient of the mid-surface $\mathbf{F}_M$ is used to map $\mathbf{m}_0$ to the current configuration.

Referring back to the kinematics of the shell element, it is obvious that the current element does not have drilling degrees of freedom. Therefore, body couples along the drilling axis (along the director vector) can not be taken into account within the variational structure of the problem. However, drilling moment would induce 'in plane' type motion and deformation which is not typically adopted in loading protocols due to its ineffectiveness in low Re locomotion of thin shell or plate like bodies.

Therefore the second term of the external virtual work is written as,

$$\int_A \delta\boldsymbol{\phi} \cdot \mathbf{q}\, t_0\, dA = \sum_{e=1}^{n_e} t_0 \int_{A_e} \delta\boldsymbol{\phi}_e \cdot \mathbf{q}_e\, dA_e \tag{35}$$

For the numerical integration of element-wise contributions (the integral in the summation sign on the right hand side) Gauss integration with three integration point is used. At each of these integration points, initial director vector is calculated through interpolation of nodal directors, similar to the director of the internal node. Afterwards, the basis vectors $\mathbf{V}_1^{ip,0}$ and $\mathbf{V}_2^{ip,0}$ at each of these integration points are obtained following the procedure outlined in Sect. 2.1. Within an increment, the body couple is decomposed into components along $\mathbf{V}_1^{ip,t}$ and $\mathbf{V}_2^{ip,t}$ so that the external virtual work can be calculated in accordance with the underlying kinematics as,

$$t_0\, \delta\underline{\phi}_e{}^T \int_{A_e} \underline{H}^T \underline{q}_e\, dA_e = \delta\underline{\phi}_e^T \underline{f}_m \text{ with} \tag{36}$$

$$\delta\underline{\phi}_e{}^T = \begin{bmatrix} \delta\alpha^1 & \delta\beta^1 & \delta\alpha^2 & \delta\beta^2 & \delta\alpha^3 & \delta\beta^3 & \delta\alpha^4 & \delta\beta^4 \end{bmatrix} \text{ and} \tag{37}$$

$$\underline{H} = \begin{bmatrix} f_1 & 0 & f_2 & 0 & f_3 & 0 & f_4 & 0 \\ 0 & f_1 & 0 & f_2 & 0 & f_3 & 0 & f_4 \end{bmatrix} \text{ and } \underline{q}_e = \begin{bmatrix} q_1 \\ q_2 \end{bmatrix} \tag{38}$$

where q_1 and q_2 are calculated at each integration point through $q_1 = \mathbf{q}_e \cdot \mathbf{V}_1^{ip}$ and $q_2 = \mathbf{q}_e \cdot \mathbf{V}_2^{ip}$. At the end of an increment, the director vector $\mathbf{V}_n^{ip}$, $\mathbf{V}_1^{ip}$ and $\mathbf{V}_2^{ip}$ of each integration point are updated as explained in Sect. 2.1.

At this stage, all the forces involved are expressed in spatially discrete form. However, an appropriate time integration scheme has to be introduced (due to dependency of $\underline{f}_d$ on $\dot{\underline{U}}_s$) and the resulting fully discrete non-linear equilibrium equations have to be solved. Time integration scheme used and the general flow of the incremental-iterative solution algorithm are presented in the "Appendix".

The outlined solution algorithm is implemented in an in-house C code which utilizes Intel Math Kernel (MKL) libraries for matrix operations and solution of equation systems. The implementation of each field solver is validated in the "Appendix" and the framework is used to analyze the swimming performance of a foldable swimmer in the next section.

3 Foldable bi-directional swimmer

The proposed foldable swimmer is composed of two arms that can rotate around internal hinges, please see Fig. 1. Grey regions are the magnetically sensitive parts of the arms and the arrows indicate the remnant magnetization directions. Arms and the middle piece are discretized by 240 elements (20×3 divisions along the edges of each arm) and 4 elements (2×1 divisions along the edges), respectively.

As far as variation of the external magnetic field is concerned, two distinct loading phases are essential. In the first phase, the external magnetic field is prescribed as $\mathbf{b} = \frac{t}{t_{p1}} b[0 \quad 0 \quad -1]^T$ where t is the current time, t_{p1} is the duration of phase 1 and b is the intensity of the magnetic field. During this phase, the arms could be forced to fully align with the external magnetic field (that is acting in $-$ z direction) by the tuning b and/or t_{p1}. In the second phase, external magnetic field oscillates in a periodic manner (T denotes the period) with a maximum angular deviation of $\pm\alpha_{rot}$ as prescribed by,

$$b_x = 0 \tag{39}$$

$$b_y = b\cos(\pi/2 + \alpha_{rot} * \sin(2\,\pi/T\,(t - t_{p1}))) \tag{40}$$

$$b_z = -b\sin(\pi/2 + \alpha_{rot} * \sin(2\,\pi/T\,(t - t_{p1}))) \tag{41}$$

The parameters of both loading phases are given in Table 1 and the complete loading history is designated as loading protocol A.

At the top row of Fig. 4, different configurations attained by the swimmer throughout the loading

Table 1 Geometry, material and external magnetic field data. The magnitude of the material data is in the order of the data used by Namdeo et al. [13]

L_e (mm)	L_m (mm)	W (mm)	B (mm)	S (mm)	t_0 (mm)
9	1	2	2	2/3	0.1
E (MPa)	ν	μ (mPa s)	b (N/(mm A))	m_r (A/mm)	
0.5	0.3	1.0	2.65×10^{-4}	62.9	

t_{p1} (s)	t_{final} (s)	T (s)	α_{rot} (rad)
1.5	3.0	3.75×10^{-2}	$\pi/6$

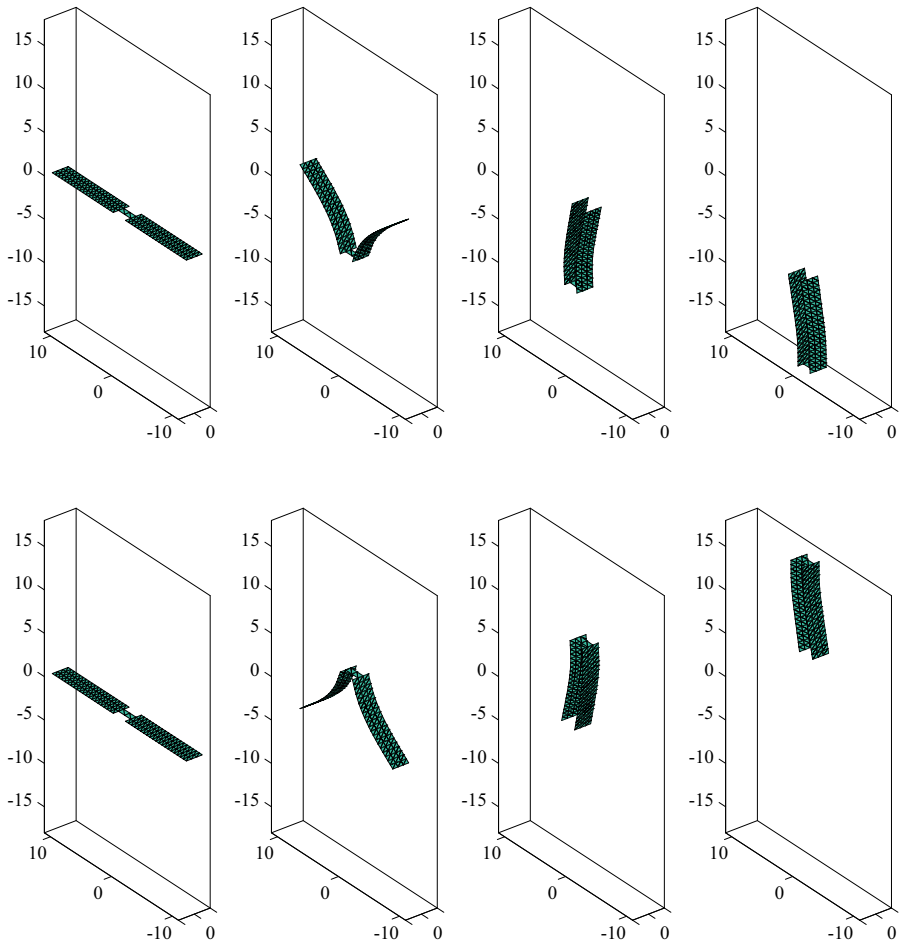

Fig. 4 Different configurations attained by the flexible two-armed swimmer throughout the loading history ($L^* = 0.1$, top row for loading protocol A and bottom row for loading protocol B)

history are shown. Initially flat horizontal arms are forced to align with the direction of the applied magnetic field during phase I, and during phase II bending induced non-reciprocal motion leads to net translation in − z direction. The evolution of the shape of the swimmer and the translation achieved are clearly visible when the planar (xy) views of the deformable body at different instants are inspected as shown at the top row of Fig. 5. Due to interaction of alternating elastic and viscous drag forces, the arms of the swimmer bend significantly during phase II which in turn breaks the symmetry and leads to net translation in − z-direction.

Swimmers that are capable of reversing their swimming direction on the fly are on demand and in fact the major novelty of the proposed swimmer addresses this sought-after feature. To highlight this capability, the same analysis is repeated simply by reversing the direction of the external magnetic field and the resulting magnetic loading is designated as loading protocol B. In other words, the magnetic field vector points in + z direction and during phase II, it oscillates around + z direction. Different configurations of the swimmer attained during loading protocol B are shown at the bottom row of Fig. 4 which clearly shows the translation in the opposite direction. Furthermore the bending dominated deformations of the swimmer and the net translation in + z direction can be clearly traced at the bottom row of Fig. 5. The translation of the body in ± z direction in the absence of an external force in z direction is remarkable. Since the linear momentum in z direction is initially zero, at any instant this has to be conserved. At this stage it is appropriate to consider the resulting flow field which is visualized at different stages of the motion in Fig. 6. The swimmer and the contours of the z-component of the flow velocity (v_z) are plotted at different instants. As far as the pattern of the velocity contour is

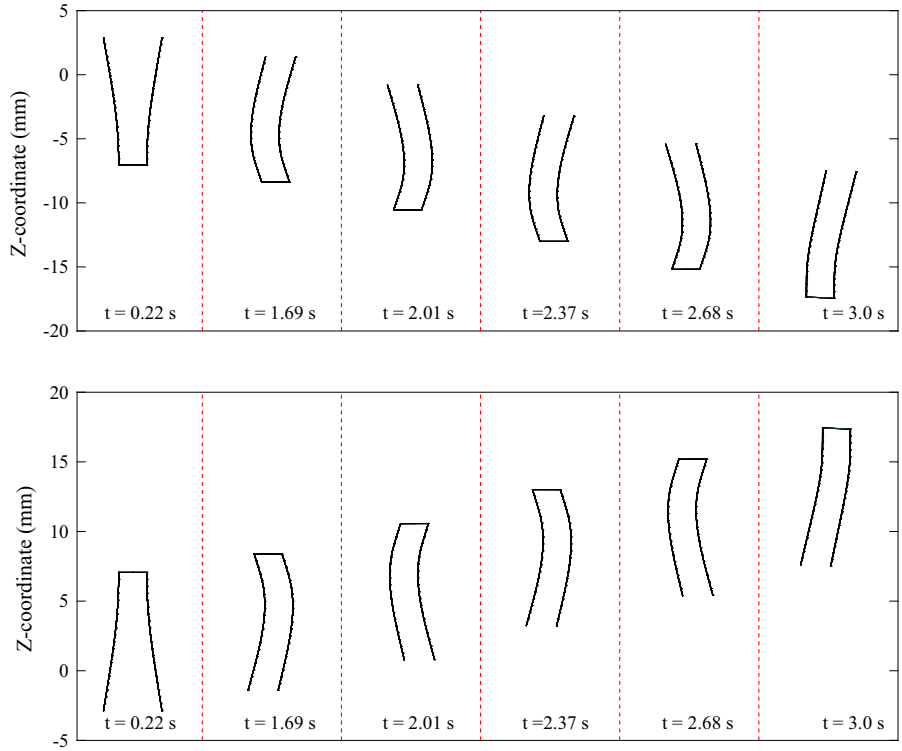

Fig. 5 Planar (xy plane) views of the swimmer at different instants. The configurations are drawn with respect to the same origin. Therefore through comparison, the net translation and the bending of the arms are clearly visible ($L^* = 0.1$, top for loading protocol A and bottom for loading protocol B)

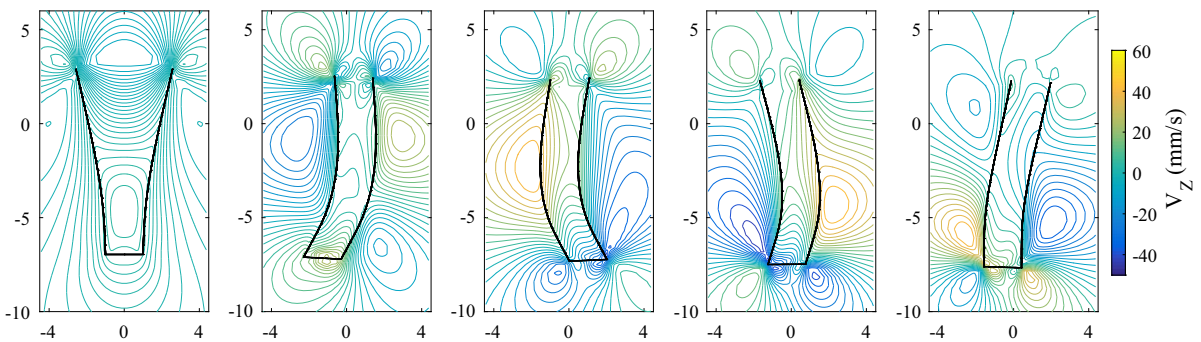

Fig. 6 z component of the flow velocity (v_z) developing around the flexible swimmer. The first snapshot represents a characteristic flow during phase I and the others are typical snapshots throughout a cycle during phase II of loading protocol A

concerned, a symmetric pattern is obtained throughout phase I as exemplified by the first contour plot. On the other hand, the magnitude of the flow velocity field evolves in such a way that the overall linear momentum of the system (flexible swimmer and the surrounding fluid domain) in z direction is conserved. Therefore during phase I, a positive flow velocity develops and during phase II an alternating fluid flow field evolves which is consistent with the instantaneous velocity of the flexible body. In other words, a net translation in − z direction implies a non-zero linear momentum for the swimmer that is counter balanced by the linear momentum of the surrounding fluid domain. Therefore the maximum and the minimum values of the velocity contour plot are typically not equal during phase II.

The z-position of the mid-point of the middle piece (please Fig. 1) is tracked throughout the motion and plotted in Fig. 7 for loading protocols A and B. In the same graph, the difference of the two loading protocols is also plotted which confirms the fact that reversing the external magnetic field leads to an

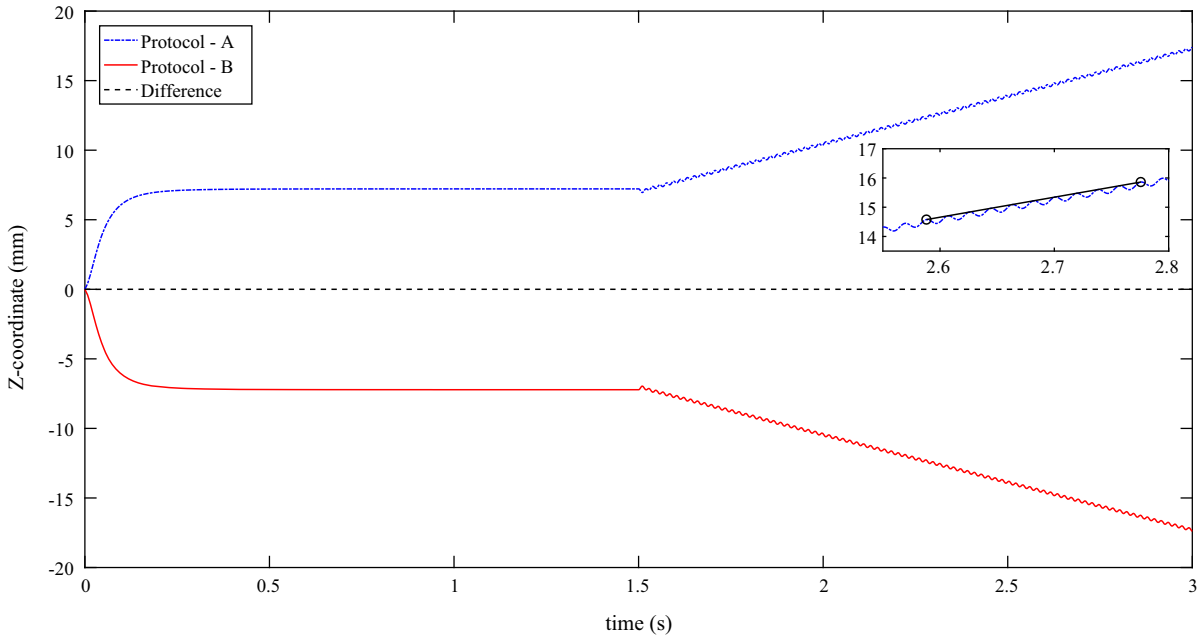

Fig. 7 Time versus Z position graph for loading protocol A and loading protocol B. Average velocity of the swimmer is based on the slope of the line segment shown in the inset

identical motion in the opposite direction. The primary performance indicator is the average translational velocity of the swimmer which is calculated from the slope of the line passing through periodic points of the cyclic graph as shown in the inset of Fig. 7. Since the motion results from the interaction of different forces, the swimming velocity depends on a number of geometric and physical parameters. To investigate the influence of each variable on the swimming performance, a set of dimensionless numbers are derived. The derivation is given in the "Appendix" and results in three dimensionless numbers,

$$L^* = \frac{L_m}{L}, M_n = \frac{12\, m_r\, b}{E}\frac{L^3}{t^2\, W}\frac{L_m}{L}\sin(\alpha_{rot}),$$
$$F_n = \frac{12\,\mu\,\omega}{E}\frac{L^4}{W\,t^3} \tag{42}$$

where F_n is the fluid number and it is the ratio of viscous forces and elastic forces whereas M_n, the magnetic number, represents the ratio of magnetic and elastic forces. A closer look at these numbers reveals that, F_n can be independently controlled by changing the viscosity μ or the frequency ω (or period) of the external magnetic field. Similarly, M_n can be controlled by varying b or m_r. Magnetically sensitive length L_m, the period (T) and the intensity b of the magnetic field are considered as variables and all the other parameters are fixed to the values given in Table 1.

First, the effect of the frequency of the external magnetic field on the resulting swimming velocity is investigated. In Fig. 8, frequency versus swimming velocity graphs are presented for three different M_n values corresponding to three different magnetic field intensities. The swimming velocity increases until a critical frequency and afterwards starts to decrease which is fully consistent with the experimental observations on magnetic micro-swimmers, see for example [16]. This critical frequency ω_c is called as step-out frequency and beyond this point the swimmer is not able to follow the externally applied oscillating magnetic field. Both the maximum speed that can be reached and the step-out frequency are increasing with the magnetic number. The loss in swimming velocity for the range $\omega > \omega_c$ is getting stronger for larger M_n values but still much milder as compared to the flexible magnetically driven swimmer presented in [13].

Obviously, the relative magnitude of the driving magnetic forces with respect to the resistive fluid forces is a major parameter controlling the response of the swimmer. In Fig. 9, swimming velocities are

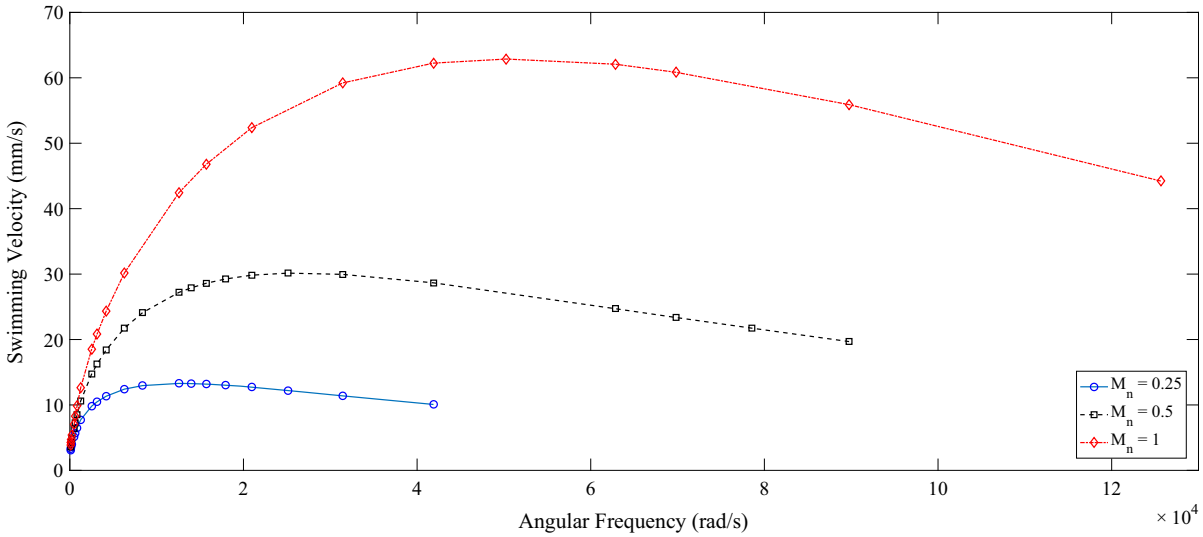

Fig. 8 Dependency of swimming velocity on the angular frequency ($2\pi/T$) of the external magnetic field for a swimmer with $L^* = 0.1$. Both maximum velocity and the step-out frequency increase with the intensity of the magnetic field

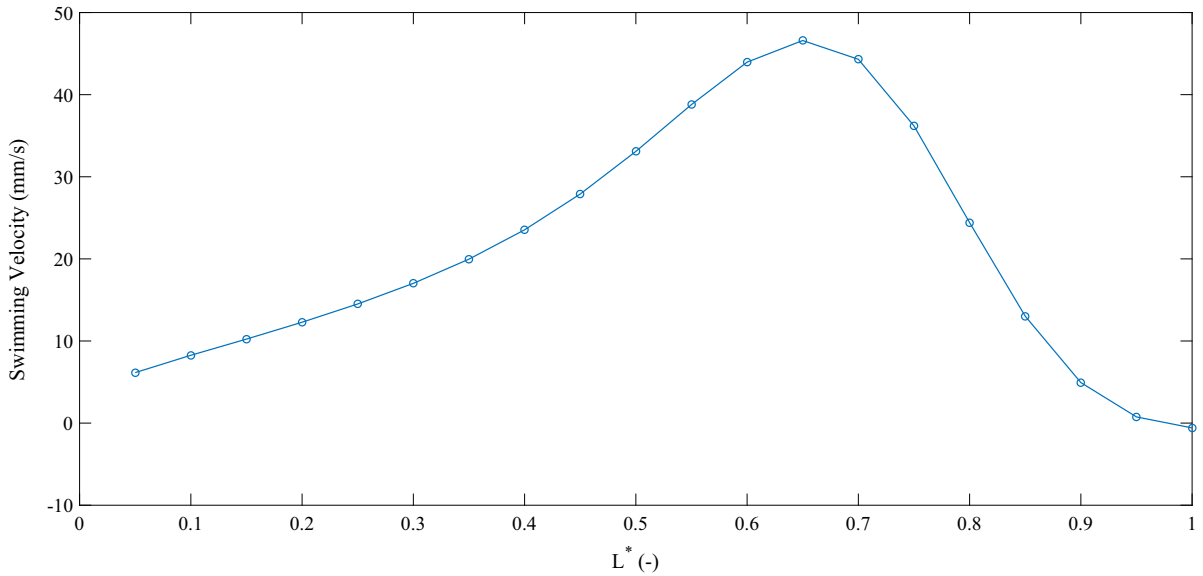

Fig. 9 Dependecy of swimming velocity on L^*. The intensity and the frequency of the magnetic field are set to $b = 2.65 \times 10^{-4}$ (N/(mm A)) and $\omega = 628.3185$ rad/s, respectively

plotted for a range of magnetic field intensities b (which in fact corresponds to increasing M_n) for three different F_n values. It is clearly seen that the swimming velocity initially increases and at a certain point the magnetic forces fully overcome the drag forces and a saturation point is reached for the swimming velocity. In other words, without modifying the elastic forces, the maximum swimming velocity achieved solely by controlling M_n, cannot be stretched any further. The upper limit for the swimming velocity increases with F_n and for larger F_n values, the saturation is delayed. Apart from F_n and M_n, L^* has a profound effect on the swimming performance as it controls both the overall distribution of magnetic moments and the available passive length of the arms that can bend. In Fig. 10, the swimming velocity is

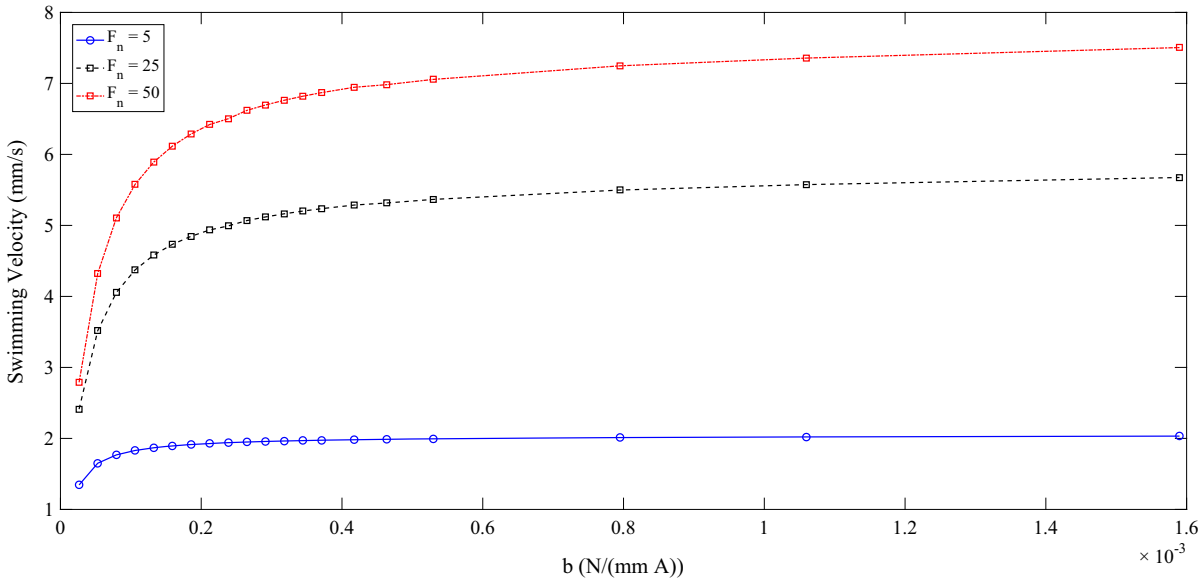

Fig. 10 Dependency of swimming velocity on the intensity of the external magnetic field for a swimmer with $L^* = 0.1$. Different F_n values correspond to three different frequencies which are all below the step-out frequency

plotted for a range of L^* values starting from $L^* = 0.05$ to $L^* = 1$. It is clearly seen that there is a critical L_c^* value beyond which the swimming velocity decreases. For $L^* > L_c^*$, the motion of the body resembles more of a ridig body as the bending deformations of the arms are becoming ineffective. This in turn severely weakens the non-reciprocal nature of the motion and the swimming velocity approaches to zero. In the extreme case of fully magnetic swimmer ($L^* = 1$), the body translates in the opposite direction with a relatively very small velocity. As proved by Purcell (scallop theorem, see [3]), in case of a single degree of freedom swimmer with rigid arms, the net displacement should be zero. Since the current model has finite stiffness and cannot be idealized as a single degree of freedom swimmer, the result obtained here is different than the theoretical limit. Although the dimensionless numbers give very valuable insight into the physics of the problem, unfortunately they do not capture the two-armed nature of the swimmer and the potential interaction between the two arms. To investigate this aspect, a set of analysis can be conducted by changing the distance B between the two arms. It has to be realized that by changing B, not only the distance between the arms but also the surface area of the middle piece is changed. With a smaller area, the drag forces acting on the swimmer are going to be modified and therefore any change in swimming velocity cannot be directly correlated to the change in spacing of the arms. However, by keeping B fixed and changing S, one can get the same area reductions for the middle piece and separate the influence of area change from the influence of arm spacing on swimming performance.

To this end, two different sets of analysis are conducted and their results are presented in Fig. 11. In the first set, the arm spacing B is modified (keeping S fixed at 0.6667 mm) such that four different cases are created with B = 0.5, 1, 2 and 4 mm, respectively. For the second set, the arms spacing B is fixed at 2 mm and S is set to 0.1667, 0.3333, 0.6667 and 1.3333 mm, respectively. As far as the area of the middle piece is concerned, each case of the first set matches with the corresponding case of the second set. If the increase in swimming velocity for both analysis sets were of the same order of magnitude then it would be possible to conclude that the spacing of the arms does not have any influence on the swimming performance. However, as seen in Fig. 11, the increase in swimming velocity obtained from the first set of analysis is much larger than the second set. Therefore the arm spacing has a very strong influence on the swimming velocity. Furthermore, larger arm spacing has an adverse effect on the resulting swimming velocity as deduced from the right tail of the curves. The trend of the curve suggests that as the spacing increases, the

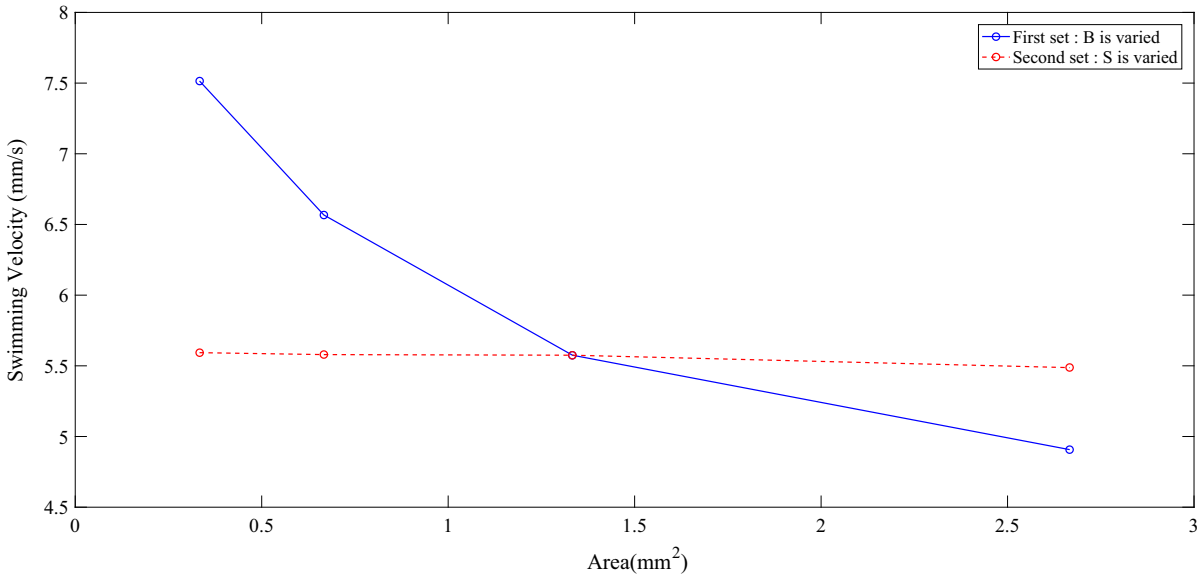

Fig. 11 Influence of arm spacing (B) and width of the middle piece (S) on the resulting swimming velocity. There are four different cases in each set of analysis and the corresponding cases (case 1 of the first set and case of the second set, etc.) yield equal surface area for the middle piece

hydrodynamic interaction between the arms ceases since the arms do not 'feel' each other anymore.

4 Conclusion and outlook

This paper has focused on interaction of low Re number flows and thin shell type deformable bodies in the context of locomotion and locomotion direction reversibility. An efficient triangular shell element based non-linear structural analysis framework and BEM type treatment of Stokes flow is coupled using the so called Dirichlet to Neumann map, see [12, 24]. The propulsion is triggered and sustained by means of body couples induced by an external magnetic field. Through the use of internal hinges, it is demonstrated that large configurational changes and bending deformations can be effectively combined and exploited to reverse the direction of locomotion. To the Author's knowledge, the use of internal hinges to reverse the locomotion direction has not been proposed before and could be a viable alternative. Furthermore, a set of dimensionless numbers reflecting the competition between different forces are identified and used to investigate the response of the swimmer.

As far as manufacturability of hinges is concerned, the thickness of polymeric strips can be locally reduced such that these regions with very small bending stiffness mimic the behavior of a frictionless internal hinge. In the numerical framework presented here, mimicking internal hinges by very thin shell elements is not pursued due to potential conditioning problem that might arise.

On the structural discretization side, rotation free formulations seem to be a very attractive alternative in the context of FSI at low Re number flows as exemplified recently by Heltai et al. [25]. However, the treatment of magnetically induced body couples in a rotation free shell formulation has to be addressed properly.

Referring back to the dimensional analysis carried out (available in the "Appendix"), as stated previously, the two-armed nature of the swimmer and hydrodynamic interaction of the two arms could not be reflected in the resulting dimensionless numbers. Although it doesn't seem to be a straight forward task, injecting the hydrodynamic interaction between different parts into the dimensional analysis of the system would be very instrumental to understand/validate the effect of arm spacing on the response of the swimmer. Definitely, smaller arm spacing call for further analysis but as demonstrated in the "Appendix", below a certain value, a very fine discretization would be necessary. Furthermore

manufacturability constraints would impose a limit on the smallest arm spacing that can be realized.

Another interesting extension could be the use of anisotropy which can be introduced through the base material of the swimmer and/or the geometric lay-out of the magnetically sensitive parts. In that case, bending-torsion coupling would be an important aspect and add a new dimension to the design space of artificial flexible micro-swimmers.

Acknowledgements This work is supported by the Scientific and Technological Council of Turkey (TÜBİTAK), Project No: 216M499. This support is gratefully acknowledged.

Appendix

Time integration and solution algorithm

For time discretization, backward Euler integration scheme is used and structural velocity field is replaced by $\dot{\mathbf{U}}^s = \frac{\mathbf{U}^s_{n+1} - \mathbf{U}^s_n}{\Delta t}$ where Δt is the time increment size. Inserting this into Eq. (33) yields,

$$\delta W_f = \int_A \delta \mathbf{u} \cdot \mathbf{t}^f \, dA = \delta \underline{\hat{u}}^T \underline{M}\, \underline{H}^{-1} \underline{A}\, \underline{\dot{U}}^s \tag{43}$$

$$\delta W_f = \delta \underline{\hat{u}}^T \underline{K}_f \left(\mathbf{U}^s_{n+1} - \mathbf{U}^s_n \right) \text{ with } \underline{K}_f = \frac{1}{\Delta t} \underline{M}\, \underline{H}^{-1} \underline{A} \tag{44}$$

Virtual work equality is enforced through the Newton–Raphson solution procedure in an incremental-iterative way. This requires consistent linearization of δW_{int} and δW_{ext} resulting in the tangent operator necessary to calculate the corrective displacements at each iteration, as summarized below.

Focusing on δW_i first, linearization of the virtual strains in the direction of incremental displacements and rotations lead to the so-called geometric tangent matrix $\underline{K}^e_g$ and the linearization of the stress components results in the material tangent stiffness matrix $\underline{K}^e_m$ of each element. The explicit forms of these matrices can be derived by following [20, 26] or [21]. The assembly of these element matrices built up the structural tangent stiffness which is denoted by $\underline{K}^s$.

Since δW_f is linear in structural displacements [see Eqs. (43) and (44)], linearization of δW_f simply yields $\underline{K}_f$ which can be interpreted as fluid stiffness. To complete the linearization procedure, δW_m has to be considered as well. Referring back to element level integral given by Eq. (35), body couple (through unit material vector **m**) and J both depend on the displacement field. Linearization of these terms can be done in a straight forward manner resulting in the associated tangent stiffness designated as $\underline{K}_m$.

Having defined individual tangent contributions, the following system of equations,

$$\begin{aligned} &\underline{r}|_k + \underline{K}_{sys}|_k d\,\underline{u}^s = \underline{0} \text{ with } \underline{r}|_k = \underline{f}_{int}|_k - \underline{f}_d|_k - \underline{f}_m|_k \\ &\text{and } \underline{K}_{sys}|_k = \underline{K}_s|_k - \underline{K}_f|_k - \underline{K}_m|_k \end{aligned} \tag{45}$$

is solved for iterative corrective structural displacements and incremental displacement column $\Delta \underline{u}^s$ is updated through $\Delta \underline{u}^s|_{k+1} = \Delta \underline{u}^s|_k + d\,\underline{u}$.

Shell element benchmark problems

To validate the implementation of the three-noded shell element (MITC3+ element), two problems are solved in this section. These problems are selected from the commonly used benchmark problems for shell element formulations, see [27]. As far as numerical integration of the element integrals is concerned, three integration points along the thickness direction and seven integration points within the mid-surface are used as suggested by Jeon et al. [19].

The first problem is the cantilever plate subjected to a shear force at the free end. Tip force is linearly increased to $P_{max} = 4.0$ in 50 steps. Material properties, dimensions and loading are shown in Fig. 12 and the plate is discretized by 256 elements. The tip displacement versus applied force graph is read from reference [19] by means of a digitizer and shown as solid line in Fig. 13. Tip displacements as obtained from the current implementation are also plotted on the same graph and the different stages of the deformation history are shown on the left-hand side of Fig. 14.

The second problem is the cantilever plate subjected to a moment at the free end. This example is considered to be a severe test to assess the large rotation capabilities of any shell element. The analytical solutions for the tip displacements for this particular problem are available and given as,

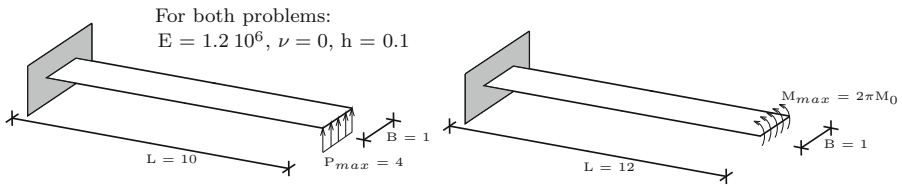

Fig. 12 Cantilever with end shear force (on the left) and with end moment (on the right)

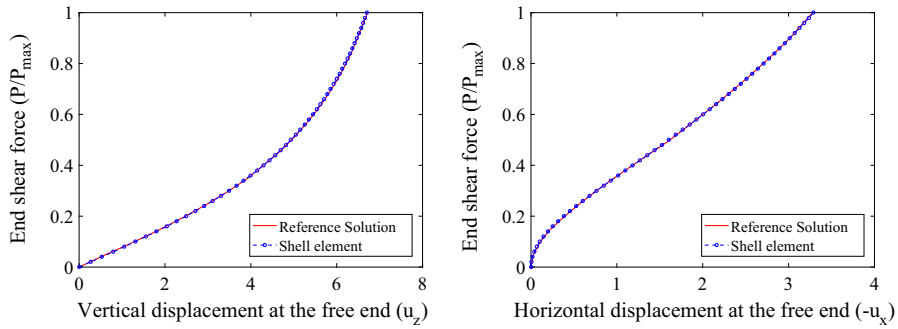

Fig. 13 Vertical and horizontal displacements at the free end of the cantilever beam

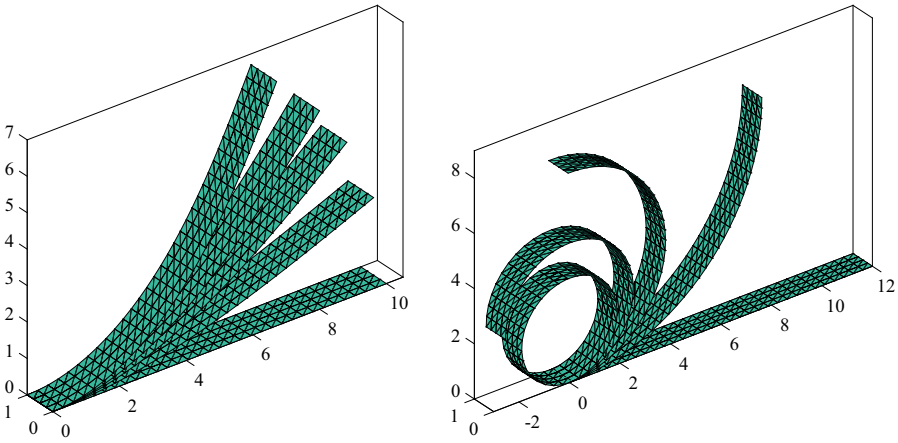

Fig. 14 Deformed configurations at different load levels for end shear force (left) and end moment (right)

$$\frac{u_x}{L} = \frac{M_0}{M}\sin\left(\frac{M}{M_0}\right) - 1 \tag{46}$$

$$\frac{u_z}{L} = \frac{M_0}{M}\left(1 - \cos\left(\frac{M}{M_0}\right)\right) \tag{47}$$

where $M_0 = \frac{EI}{L}$ and M is the applied moment. In this problem, applied moment reaches to the maximum value of $2\pi M_0$ linearly in 100 steps, resulting in a complete circular strip at the end of loading history. Problem data is given in Fig. 12 and the deformed configuration at different load levels are shown on the right-hand side of Fig. 14. Cantilever plate is discretized by 256 elements and the tip displacements as obtained from the current implementation along with the analytical solutions are plotted in Fig. 15. These two examples clearly demonstrates the validity of the current implementation and highly accurate predictive capabilities of the MITC3+ element.

Boundary element benchmark problems

Referring back to equation (29) and assembly of $\underline{H}$ matrix, element level contributions $\int_{A^e} \underline{G}\,\underline{N}\,dA_e$ have to be evaluated. Since this integral links the traction acting on an element and induced velocity at all the nodes of the shell mid-surface, $1/R$ type singularity arises for the nodes of the element under

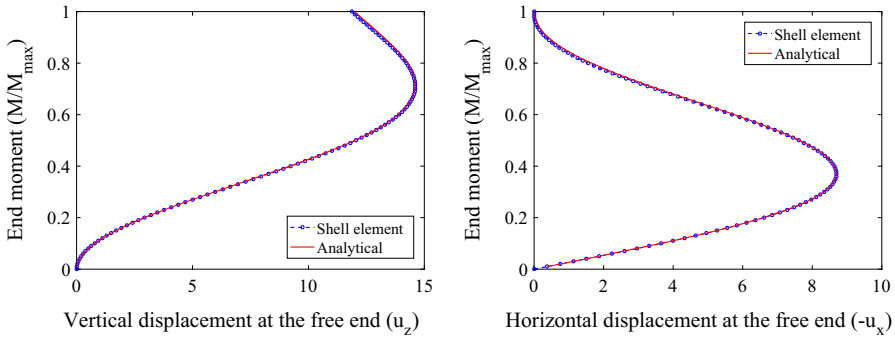

Fig. 15 Vertical and horizontal displacements at the free end of the cantilever beam

consideration. This singularity is circumvented by introducing polar coordinates in the plane of the triangular element and rewriting the integral in an alternative trigonometric form as detailed in section 5.2.2 of [22]. After the transformation, the singularity disappears and the resulting trigonometric integrands are evaluated by Gauss integration with 50 points. For non-singular cases, original element integrals (without polar coordinate transformation) are evaluated by Gauss integration with 13 points.

To validate boundary element based determination of drag tractions, two variants of a well-known problem are considered. In the first case, translation of a sphere in an unbounded fluid domain is considered. The analytical value for the drag force is given as $F_D = 6\pi\,\mu\,r\,V$ (Stokes drag formula) where μ is the viscosity, r is the radius and V is the translational velocity of the sphere.

A sphere of radius $r = 0.1$ is discretized and a translational velocity of $V_x = 0.5, V_y = 0, V_z = 0$ is imposed on the surface of the sphere as it moves in a stationary fluid of $\mu = 2$. Both structured and unstructured meshes are considered, please see Fig. 16 for representative meshes. At the end of the analysis, the resulting nodal reaction forces are summed up component-wise in respective directions. Percentage error in the calculated drag forces is plotted for various unstructured discretizations in Fig. 17. Furthermore, the drag forces in the other two directions, which are supposed to be zero are plotted on the right hand side of Fig. 17. (Different values for F_x and F_z are due to unstructured meshes used here.)

In the second case, translation of a sphere along a no-slip homogeneous infinite wall is considered. In principle, existence of a no-slip wall can be embedded in the Green's function, see e.g. [28], and therefore discretization of the wall can be circumvented. However, at the end of loading phase I, the arms of the swimmer become parallel and they start to act as finite sized no-slip obstacle/plane for each other. Therefore the benchmark problem is solved by explicitly discretizing the no-slip wall. In Fig. 18, the geometric lay-out of the problem is shown. Based on the parametric analysis results given in [29], the

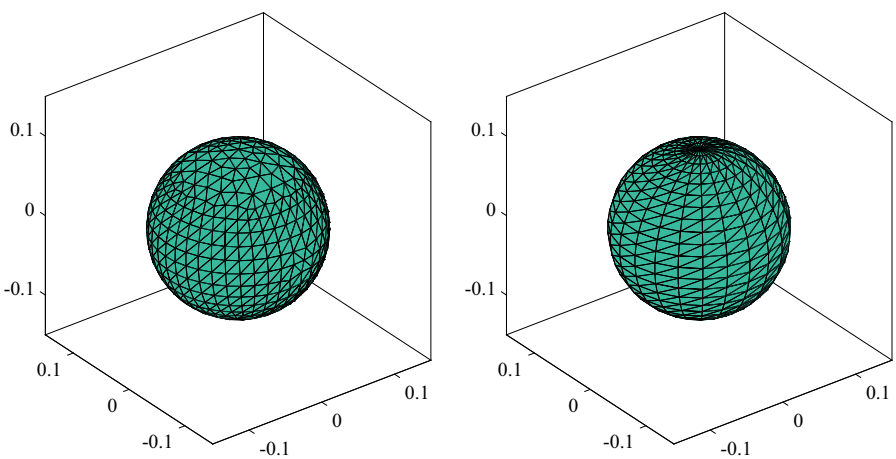

Fig. 16 Representative unstructured (left) and structured (right) meshes for the translating sphere problem

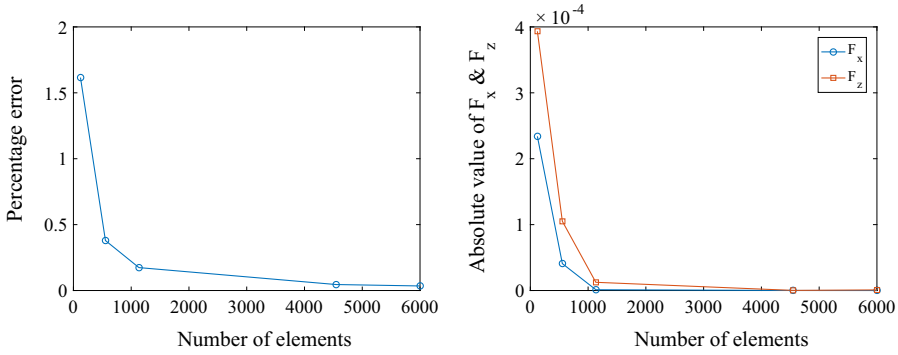

Fig. 17 Discretization versus error graphs for unstructed meshes

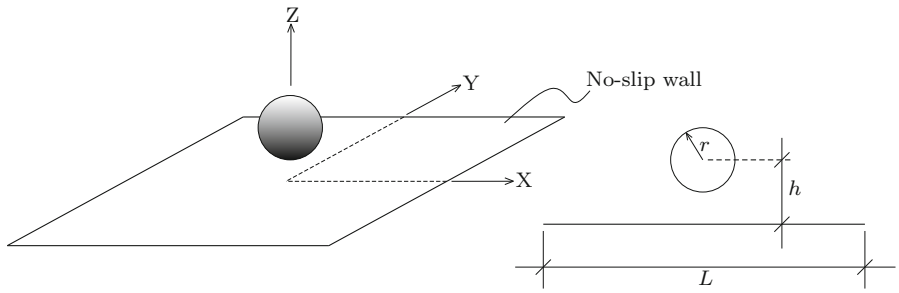

Fig. 18 3D (left) and 2D (right) geometric lay-outs for the translating sphere close to a no-slip rigid wall problem

infinite wall is truncated with a side length L of $32\,r$ and discretized by triangular shell elements. Zero velocity conditions are imposed on the wall and the sphere is translated in X-direction with $V_x = 1.0, V_y = 0, V_z = 0$. While the discretization of the sphere is fixed (a structured mesh of 1624 elements), two different structured meshes (mesh 1: 40 by 40, mesh 2: 50 by 50 divisions along the edges of the wall) and an unstructured (mesh 3: locally refined below the sphere; 3650 triangular elements) mesh are used for the wall. The resulting dimensionless drag force R^* (drag force in X-direction is scaled by $6\,\pi\,\mu\,r\,V_x$) for different h/r are plotted in Fig. 19 along with the reference solutions taken from [30]. The agreement between the numerical predictions and the reference solution is very good provided that $h/r > 1.1276$. For $h/r = 1.0453$ and $h/r = 1.1276$, mesh convergence trend is shown on the right-hand side of Fig. 19 and can be concluded that a dedicated locally refined mesh has to be used if very accurate predictions are required when the sphere is very close to the plate.

There results clearly indicate the accuracy of the method and support the adequacy of the number of integration points used.

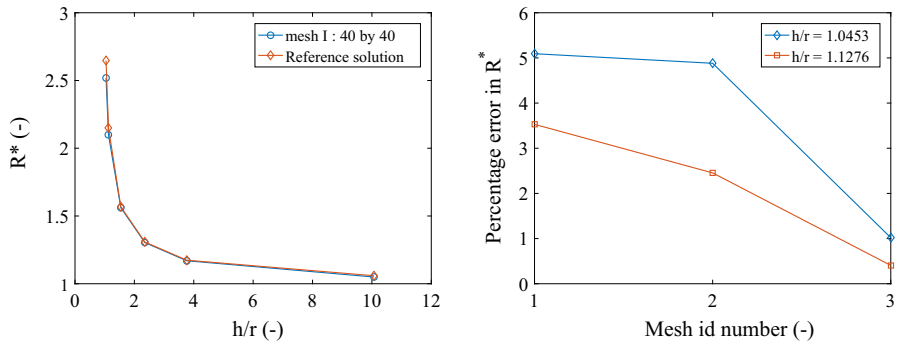

Fig. 19 Left: h / r versus dimensionless drag force R^* graph (reference solution is taken from [30]) and, right: percentage error in R^* for different meshes

Dimensional analysis

The following analysis follows the framework presented in [13] and focuses on the forces acting on one arm of the swimmer during phase II of the loading protocol. Since the dominant mode of deformation is uni-axial bending, in-plane deformations can be ignored and the virtual work equation can be simplified as,

$$\int_0^L \int_0^W \delta\kappa\, M\, dA = \int_0^L \int_0^W t^f\, \delta u_z\, dA + \int_0^{L_m} \int_0^W M_m\, \delta\beta\, t\, dA \tag{48}$$

where u_z is the transverse displacement component, M_m is the magnetic moment and β is the work conjugate rotation field, i.e. rotation around X-axis, please see Fig. 1. κ is the curvature and governed by $\kappa = \frac{M}{EI}$. In case of negligible transverse shear deformations, the change in β is proportional to $\int \kappa\, dy$ and in turn u_z is proportional to $\int \beta\, dy$. Therefore for a fixed shell thickness, β and u_z scale with L/W and L^2/W, respectively. Therefore the dimensionless transverse displacement u_z^* is introduced as, $u_z^* = u_z\, W/L^2$ or $u_z = L^2/W\, u_z^*$ and $\delta u_z = L^2/W \delta u_z^*$. Furthermore the following dimensionless parameters,

$$x = x^* L, y = y^* W \tag{49}$$

$$A = A^* L\, W (\text{or } A = A^* L_m W \text{ for the magnetic part}) \tag{50}$$

are used in the subsequent steps. Due to dimensional considerations, t^f should be proportional to $\mu\, u_z^*\, \omega$ where ω is the frequency of the external magnetic field (The dimension of $u_z^*\, \omega$ is $-$/time akin to velocity gradient). Lastly, the magnetic moment M_m can be expressed as $M_m = m_r\, b \sin(\alpha)$ where α is the angle between **m** and **b** vectors. Considering α_{rot} as the characteristic value for α, the virtual work equality can eventually be re-written as,

$$\frac{E\, W\, t^3}{12\, L} \int_0^1 \int_0^1 \kappa^* \delta\kappa^*\, dA^* = \mu\, \omega\, L^3 \int_0^1 \int_0^1 u_z^*\, \delta u_z^*\, dA^* + m_r\, b\, t\, L\, L_m \sin(\alpha_{rot}) \int_0^1 \int_0^1 \delta\beta\, dA^* \tag{51}$$

Scaling the pre-multipliers appearing on the right-hand side by the one on the left-hand side yields the dimensionless numbers M_n and F_n written as;

$$M_n = \frac{12\, m_r\, b}{E} \frac{L^3}{t^2\, W} \frac{L_m}{L} \sin(\alpha_{rot}), F_n = \frac{12\, \mu\, \omega}{E} \frac{L^4}{W\, t^3} \tag{52}$$

$\frac{L_m}{L}$ has to be considered as a separate governing dimensionless number and its influence on M_n is clearly visible.

References

1. Gao W, Kagan D, Pak O, Clawson C, Campuzano S, Chuluun-Erdene E, Shipton E, Fullerton E, Zhang L, Lauga E, Wang J (2012) Cargo-towing fuel-free magnetic nanoswimmers for targeted drug delivery. Small 8(3):460. https://doi.org/10.1002/smll.201101909
2. Lauga E, Powers T (2009) The hydrodynamics of swimming microorganisms. Rep Prog Phys 72(9):096601. https://doi.org/10.1088/0034-4885/72/9/096601
3. Purcell E (1977) Life at low Reynolds number. Am J Phys 45:3. https://doi.org/10.1119/1.10903
4. Gray J, Hancock J (1955) The propulsion of sea-urchin spermatazoa. J Exp Biol 32:802
5. Rodenborn B, Chen CH, Swinney H, Liu B, Zhang H (2013) Propulsion of microorganisms by a helical flagellum. Proc Natl Acad Sci USA. https://doi.org/10.1073/pnas.1219831110
6. Johnson R, Brokaw C (1979) A comparison between resistive force theory and slender-body theory. Biophys J 25:113. https://doi.org/10.1016/S0006-3495(79)85281-9
7. Lighthill J (1976) Flagellar hydrodynamics. SIAM Rev 18:161. https://doi.org/10.1137/1018040
8. Pozrikidis C (2011) Shear flow past slender elastic rods attached to a plane. Int J Solids Struct 48:137. https://doi.org/10.1016/j.ijdpldtr.2010.09.012
9. Cortez R (2001) The method of regularized stokeslets. SIAM J Sci Comput 23:1204. https://doi.org/10.1137/S106482750038146X
10. Cortez R, Fauci L, Medovikov A (2005) The method of regularized stokeslets in three dimensions: analysis, validaiton and application to helical swimming. Phys Fluids 17:031504. https://doi.org/10.1063/1.1830486
11. Namdeo S, Khaderi S, den Toonder J, Onck P (2011) Swimming direction reversal of flagella through ciliary

motion of mastigonomes. Biomicrofluidics 5:034108. https://doi.org/10.1063/1.3608240
12. Khaderi S, Onck P (2012) Fluid–structure interaction of three-dimensional magnetic artificial cilia. J Fluid Mech 708:303. https://doi.org/10.1017/jfm.2012.306
13. Namdeo S, Khaderi S, Onck P (2014) Numerical modelling of chirality-induced bi-directional swimming of artificial flagella. Proc R Soc A 470:20130547. https://doi.org/10.1098/rspa.2013.0547
14. Dreyfus R, Baudry J, Roper M, Fermigier M, Stone H, Bibette J (2005) Microscopic artificial swimmers. Nature 437:862. https://doi.org/10.1088/0953-8984/21/20/204110
15. Alouges F, DeSimone A, Giraldi L, Zoppello M (2013) Can magnetic multilayers propel microswimmers mimicking sperm cell? Soft Robot 2(3):117. https://doi.org/10.1088/0953-8984/21/20/204110
16. Qiu F, Fujita S, Mhanna R, Zhang L, Simona BR, Nelson BJ (2015) Magnetic helical microswimmers functionalized with lipoplexes for targeted gene delivery. Adv Funct Mater 25:1666. https://doi.org/10.1002/adfm.201403891
17. Yeo Z, Regnier S, Sitti M (2014) Rotating magnetic miniature swimming robots with multiple flexible flagella. IEEE Trans Robot 30–1:3. https://doi.org/10.1109/TRO.2013.2280058
18. Lee Y, Lee PS, Bathe K (2014) The MITC3+ shell element and its performance. Comput Struct 138:12. https://doi.org/10.1016/j.compstruc.2014.02.005/
19. Jeon HM, Lee Y, Lee PS, Bathe K (2015) The MITC3+ shell element and its performance. Comput Struct 146:91. https://doi.org/10.1016/j.compstruc.2014.09.004/
20. Bathe K (1996) Finite element procedures. Prentice-Hall, Inc., Upper Saddle River
21. Bucalem M, Bathe K (1997) Finite element analysis of shell structures. Arch Comput Methods Eng 4:3
22. Pozrikidis C (1992) Boundary integral and singularity methods for linearized viscous flow. Cambridge University Press, Cambridge
23. Khaderi S (2011) Nature-inspired microfluidic propulsion using magnetic artificial cilia. Phd Thesis, University of Groningen
24. Giuliani N, Heltai L, DeSimone A (2018) Predicting and optimizing microswimmer performance from the hydrodynamics of its components: the relevance of interactions. Soft Robot 5(4):410. https://doi.org/10.1089/soro.2017.0099
25. Heltai L, Kiendl J, DeSimone A, Reali A (2017) A natural framework for isogeometric fluid–structure interaction based on BEM-shell coupling. Comput Methods Appl Mech Eng 316:522. https://doi.org/10.1016/j.cma.2016.08.008
26. Dvorkin E (1984) On non-linear finite element analysis of shell structures. Massachusetts Institute of Technology
27. Sze K, Liu X, Lo S (2004) Popular benchmark problems for geometric nonlinear analysis of shells. Finite Elem Anal Des 40:1551. https://doi.org/10.1016/j.finel.2003.11.001
28. Blake J (1971) A note on the image system for a stokeslet in a no-slip boundary. Math Proc Camb Philos Soc 70(02):303. https://doi.org/10.1017/S0305004100049902
29. Pimponi D, Chinappi M, Gualtieri P, Casciola C (2014) Mobility tensor of a sphere moving on a superhydrophobic wall: application to particle separation. Microfluidics Nanofluidics 16:571. https://doi.org/10.1007/s10404-013-1243-4
30. Goldman A, Fox R, Brenner H (1967) Slow viscous motion of a sphere parallel to a plane. Chem Eng Sci 22:637. https://doi.org/10.1016/0009-2509(67)80047-2